Title

Quantification of strain and its impact on the phase stabilization of all-inorganic cesium lead iodide perovskites

Journal

Matter, 6(7)

ISSN

2590-2393

Authors

Le, Han KD
Lin, Chung-Kuan
Jin, Jianbo
et al.

Publication Date

2023-07-01

DOI

10.1016/j.matt.2023.05.027

Peer reviewed

Quantification of strain and its impact on the phase stabilization of all-inorganic cesium lead iodide perovskite

Han K. D. Le[1,2], Chung-Kuan Lin[1,2], Jianbo Jin[1], Ye Zhang[1], Zhenni Lin[2,3], Arturas Vaillionis[4,5], Nobumichi Tamura[6], Peidong Yang[1,2,3,7,8,*]

[1]Department of Chemistry, University of California, Berkeley, CA 94720, USA.

[2]Materials Sciences Division, Lawrence Berkeley National Laboratory, Berkeley, CA 94720, USA.

[3]Department of Materials Science and Engineering, University of California, Berkeley, CA 94720, USA.

[4]Stanford Nano Shared Facilities, Stanford University, Stanford, CA 94305, USA.

[5]Department of Physics, Kaunas University of Technology, LT-51368 Kaunas, Lithuania.

[6]Advanced Light Source, Lawrence Berkeley National Laboratory, Berkeley, CA 94720, USA.

[7]Kavli Energy Nano Science Institute, Berkeley, CA 94720, USA.

[8]Lead Contact. Email: p_yang@berkeley.edu (P.Y.)

*Corresponding Author. Email: p_yang@berkeley.edu (P.Y.)

Summary

The high-temperature perovskite γ-phase of $CsPbI_3$ readily undergoes phase transition at ambient conditions to a low-temperature non-perovskite δ-phase with a poorer optoelectronic performance, thus hindering commercialization of these materials in photovoltaics. Here, we present the epitaxial growth of $CsPbI_3$ nanoplates on muscovite mica single crystal substrates, and demonstrate that the high-temperature phase stability of these nanoplates is enhanced by a strained interface. Strain is measured as a function of nanoplate thickness on a single particle level through spatially resolved structural and optical characterizations, and found to increase with decreasing thickness. From quantitatively tracking the $CsPbI_3$ phase transition for thin (<400 nm) and thick (>400 nm) nanoplates, we observe a larger fraction of thin nanoplates still maintaining their high-temperature phase after one month as compared to the thick counterparts. These findings establish a relationship between strain and phase transition kinetics, which is critical for rational design of stable perovskite-based optoelectronic devices.

Keywords: metal halide perovskites, phase transition, structural transformation, strain, epitaxial growth, quantitative imaging

Introduction

Halide perovskites have emerged as an exciting class of materials and garnered significant interest for its impressive performance in photovoltaic technologies, with power conversion efficiencies (PCEs) of perovskite solar cells (PSCs) increasing from 3.8%[1] to a certified 25.2%[2] and rivaling commercial silicon solar cells in recent years.[3,4,5] A type of all-inorganic perovskite,

cesium lead iodide ($CsPbI_3$) draws special attention owing to its suitable bandgap for photovoltaics (~1.73 eV)[6,7] and its superior thermal tolerance as compared to the organic-inorganic hybrid counterparts.[8,9] Despite these advantages, a main obstacle to realizing the commercial applications of these materials lies in the long-term phase instability and interconversion between different $CsPbI_3$ polymorphs.[10–12] $CsPbI_3$ readily undergoes phase transition at ambient conditions from a metastable, high temperature (high-T) perovskite ɣ-phase to an unfavorable, low temperature (low-T) non-perovskite δ-phase, which has a larger bandgap (~2.82 eV) and is not suitable for solar cell applications.[13–17] Therefore, it is crucial to understand this phase transition and develop strategies to stabilize the high-T perovskite phase for practical $CsPbI_3$-based device applications.

Among factors affecting the phase stability of perovskites, strain has been found to play a significant role.[18–23] Understanding the effect of strain on perovskites is particularly relevant and necessary, as the soft lattice nature of perovskites enables them to be highly susceptible to strain.[21,24,25] Strain has been extensively studied for several perovskite compositions and employed to tune the stability of perovskite films, thereby enhancing optoelectronic properties and device performances.[18–21,26–28] For instance, through strain management, a certified PCE of ~24.4% has been reported for $FAPbI_3$-based PSCs (where FA is formamidinium).[28] Residual strain engineering has been demonstrated to achieve improvement in hole carrier transport and extraction, resulting in optimized mixed $(FAPbI_3)_{0.85}(MAPbBr_3)_{0.15}$ PSCs with a certified PCE of 20.7%.[29] Strain engineering of perovskites is typically achieved through the selection of a suitable substrate on which epitaxial growth of the perovskite layer can occur. Epitaxy refers to the growth of a crystalline epilayer on a crystalline substrate where the epilayer exhibits well-

defined orientations relative to the substrate's crystal orientations. A strained epilayer can form to accommodate the in-plane lattice parameters of the substrate if the lattice mismatch is not too large. For instance, lattice strain has been reported to exist in α-$FAPbI_3$ thin films epitaxially grown on a series of $MAPbCl_xBr_{3-x}$ single crystalline substrates. Further tuning of the composition of the $MAPbCl_xBr_{3-x}$ substrate introduces different levels of strain to the α-$FAPbI_3$ epilayer, and the resultant strain is found to have a stabilization effect on the α-$FAPbI_3$ phase.[18] Steele *et al.*[26] investigated strain in $CsPbI_3$ thin films and showed that strain reduces the energy difference promoting the high-T-to-low-T phase transition, thus rendering the high-T phase stable at room temperature. On the other hand, strain has also been observed in $MAPbI_3$ polycrystalline films but in this case proves to be detrimental to film stability under illumination.[19] Thus, opposite strain-induced effects are exhibited in similarly strained perovskites, necessitating the need to thoroughly study strain across all classes of perovskite materials. Although strain engineering has been extensively investigated in polycrystalline perovskite thin films, a systematic investigation of strain and its influence on the phase stability of the model all-inorganic single-crystalline $CsPbI_3$ is still lacking. The strain distribution within these single crystals grown on single crystalline substrates might differ from that within polycrystalline thin films, where the presence of grain boundaries and film edges can be a major contributing source.[24] Considering the broad range of impacts induced by strain, a fundamental understanding of the intrinsic strain properties and its influence on phase stability of $CsPbI_3$ single crystals is critical to lay the foundations for further thin film preparation and optimization of $CsPbI_3$ solar cell devices.

In this work, we report the highly oriented growth of $CsPbI_3$ single crystalline nanoplates with different thicknesses on muscovite mica single crystal substrates with a well-defined epitaxial relationship. We systematically characterize and quantify the intrinsic lattice strain associated with varying nanoplate thicknesses at a single particle level using a combination of structural and optical techniques with localized microscale probing. These spatially resolved techniques allow us to precisely determine any strain-induced changes within individual nanoplates and overcome the common issue of averaging out sample heterogeneity (e.g, thickness, morphology) in conventional characterization methods. We demonstrate that the strained epitaxy can enhance the phase stability of metastable high-T $CsPbI_3$ nanoplates for at least one month under ambient conditions (50% ± 2% RH, 21 ± 1°C). Lastly, we discuss the origin of this intrinsic lattice strain and the observed strain-induced phase stabilization. These findings establish an understanding of epitaxial growth and the effect of strain on phase transitions at the single crystal level, thereby driving the design and optimization of long-term, highly phase-stable perovskite materials and devices.

Results and Discussion

The epitaxial growth of $CsPbI_3$ perovskite nanoplates on muscovite mica was carried out using chemical vapor transport (CVT) method (see Experimental Method for more details regarding the experimental growth setup and conditions). The as-grown nanoplates have thicknesses ranging from 180 nm to 1.5 μm, which can be measured using atomic force microscopy (AFM) (Figure 1A) and identified through the color differences in the optical microscope image (Figure 1C). Figure 1B shows a few representative height profiles generated from AFM measurements of

the nanoplates. All the nanoplates have a rectangular/square morphology with lateral dimensions of 5-12 μm, and are well-oriented at multiples of 90°, indicating the well-defined epitaxial growth of these crystals on the mica substrate (Figure 1C, Figure S1-S2). Energy-dispersive X-ray spectroscopic (EDX) measurements confirmed the atomic ratio of Cs:Pb:I to be approximately 1:1:3 for $CsPbI_3$ nanoplates of different thicknesses (Figure S3).

The van der Waals epitaxial growth of halide perovskites nanostructures on mica is facilitated by the chemically inert nature of the substrate that relaxes strict lattice matching conditions.[30–33] The structure of muscovite mica is consisted of positively charged K^+ inserted between adjacent negatively charged tetrahedral aluminosilicate layers. These adjacent aluminosilicate sheets in mica are connected by weak van der Waals forces; thus, mica can be easily exfoliated along the K^+ layer, resulting in an atomically flat surface without any dangling bonds.[22,30,31] The cubic $CsPbBr_3$ nanoplates have been found to epitaxially grow on the (001) surface of muscovite mica with the (001) facet exposed and in-plane orientations of $CsPbBr_3$[100]//mica[100] and $CsPbBr_3$[010]//mica[010].[30] Although the interface between cubic $CsPbBr_3$ and mica substrates is well-studied in the literature,[30–33] to date there has been no characterization on the epitaxial relationship between mica and the orthorhombic γ-phase $CsPbI_3$, which has a lower symmetry and different lattice parameters. To determine the crystallographic orientation of the $CsPbI_3$ nanoplates with respect to the muscovite mica substrate, two X-ray pole figures were acquired at $2\theta = 27.84^o$ and 29.85^o for mica (114) and $CsPbI_3$ (221), respectively (Figure 1D, Figures S4-S5). The diffracted intensity was measured by varying the tilt angle, ψ, and the rotation angle, φ, with respect to the normal to the sample surface while holding 2θ constant. The mica{114} pole

figure exhibits six equidistant poles at a tilt angle $\psi = 45.125^{o}$ and $\Delta\varphi = 60^{o}$. This is because mica has two twin domains, with one domain producing four {114} poles at $\varphi = 18.4^{o}$, 78.4^{o}, 198.4^{o} and 258.4^{o}, and the other domain producing four {114} poles at $\varphi = 78.4^{o}$, 138.4^{o}, 258.4^{o}, 318.4^{o} (Figure S6). For the {221} $CsPbI_3$ pole figures, we observed 8 total poles at a tilt angle $\psi = 13.874^{o}$. $CsPbI_3$ can align in two symmetrically equivalent orientations rotated by 90^{o} on mica. Each of these $CsPbI_3$ orientations results in a set of 2 poles, (221) and ($22\acute{1}$), which are separated at an azimuthal interval of 180^{o}. Thus, for each of the twin domains of mica, there would be 4 equivalent {221} $CsPbI_3$ poles equally spaced at 90^{o}. One of the twin domains forms one set of 4 stronger intensity {221} $CsPbI_3$ poles that are more energetically favorable, while the other domain produces another set of 4 weaker intensity {221} $CsPbI_3$ poles. The measured pole figures match well with the simulations of the mica{114} and $CsPbI_3${221} pole figures (Figures S6-S7). From the pole figures, we proposed an incommensurate epitaxial relationship between the as-grown $CsPbI_3$ nanoplates and the mica substrate. The [110] direction of the nanoplates is parallel to the [001] direction of muscovite mica in the out-of-plane direction, and the [$\acute{1}$12] direction of the nanoplates is parallel to the [110] direction of mica in the in-plane direction (Figure 1E). The out-of-plane orientation is consistent with previous studies of cubic $CsPbBr_3$ on mica, as the orthorhombic{110} facet is equivalent to cubic{001} crystal planes with slight distortion. Along the in-plane direction, one periodicity of $CsPbI_3$[$\acute{1}$12] approximately matches with one periodicity of mica[110], with a lattice mismatch factor f of -2.89% ($f = \frac{d_{overlayer}}{d_{substrate}} - 1$). This lattice mismatch can result in lattice strain and suggest that the lattice of $CsPbI_3$ is dilated along the in-plane direction at the perovskite-mica interface in order to match with the mica

lattice. A strong ionic interaction between the K^+ layer from mica and the I^- from the PbI_2 layer of $CsPbI_3$ is expected,[32] which might serve as a driving force to generate the in-plane tensile strain in order to resolve the lattice mismatch.

Figure 2A shows the powder X-ray diffraction (PXRD) pattern of the as-grown $CsPbI_3$ nanoplates on muscovite mica. The mica substrate has a monoclinic lattice and displays equally spaced diffraction peaks corresponding to the exposed (00l) planes (a = 5.211 Å, b = 9.040 Å, c = 20.021 Å, $\alpha = \gamma = 90^o$, $\beta = 95.76^o$). The perovskite nanoplates show predominant diffraction peaks at 14.39° and 29.00°, which can be indexed to the (110) and (220) planes of orthorhombic γ-phase $CsPbI_3$ (space group: *Pnma*, a = 8.856 Å, b = 8.577 Å, c = 12.472 Å, $\alpha = \beta = \gamma = 90^o$). The dominance of these peaks indicates that the [110] direction of the nanoplates is normal to the mica (001) substrate. The absence of other diffraction peaks from the high-T phase confirms the highly oriented growth of the nanoplates on the (001) surface of mica.

A change in d-spacing through Bragg peak positions of a PXRD pattern is expected as an indication of strain in a material.[21] If a material is compressively strained, the d-spacing is decreased relative to the strain-free reference, and the associated Bragg peak will shift to a higher 2θ angle (and vice versa for tensile strain). The strain value (ε) can be calculated from this XRD peak shift and expressed as a percentage with respect to the reference or non-strained sample, with negative/positive sign indicating compressive/tensile strain, respectively:

$$\varepsilon = \frac{d_{strained(hkl)} - d_{non-strained(hkl)}}{d_{non-strained(hkl)}}$$

where $d_{strained(hkl)}$ and $d_{non-strained(hkl)}$ are the crystal plane spacing of perovskites with and without strain.[35] We observe that the Bragg peak associated with the (110) plane for the $CsPbI_3$ nanoplates grown on mica shifts towards a higher 2θ as compared to that of bulk, free-standing γ-phase $CsPbI_3$ powder from Sutton *et al*,[34] indicating a decreased d-spacing in the [110] direction relative to the reference (Figure 2B). This suggests that the plates grown on mica have a compressive strain in the out-of-plane direction, and this strain is calculated to be -0.2%. We also note that $CsPbI_3$ nanoplates randomly grown on an amorphous Si/SiO_2 substrate (Figure S8) show a diffraction peak at 14.36°, thus not displaying any Bragg peak shift for the (110) plane as compared to the reference value (Figure 2B, Figure S10). As a result, we can consider the $CsPbI_3$ nanoplates on Si/SiO_2 substrates as the strain-free reference. The fact that we were able to observe a peak shift for the nanoplates grown on single crystal mica substrate but not on the amorphous Si/SiO_2 substrate indicates that the observed strain is associated with the perovskite-mica interaction. Conventional PXRD techniques measure a large region and average out any heterogeneity within the sample due to a large area X-ray spot size (1-5 millimeters). It is crucial to note that our aforementioned powder XRD measurement of $CsPbI_3$ on mica was conducted on a large region of nanoplates of various thicknesses with different levels of strain; therefore, the calculated out-of-plane strain is an averaged value. Synchrotron X-ray microdiffraction (μXRD) can probe nanoplates one at a time with an X-ray beam of a few micrometers, thus allowing us to determine any strain-induced lattice changes between plates of different thicknesses. To further verify our strain hypothesis, we conducted Laue μXRD to characterize the crystal structure, crystallographic orientation and strain of individual nanoplates of various thicknesses with micrometer resolution. Regions of nanoplates of interest are located with X-ray micro-

fluorescence mapping (Figure S11), and Laue patterns can subsequently be obtained for each individual nanoplate. A representative Laue pattern from a single nanoplate is shown in Figure 2C. From the Laue pattern, we were able to index the Laue reflection spots to orthorhombic γ-phase $CsPbI_3$. The locations of the Laue reflection spots allow determination of the crystal orientation and further confirm the epitaxial relationship between the perovskite and mica substrate previously determined with X-ray pole figure. The mica[001] and $CsPbI_3$[110] are exactly aligned in the out-of-plane direction, and the mica[110] and $CsPbI_3$[1̄12] are aligned in the in-plane direction, as seen from the stereographic projections of several individual $CsPbI_3$ nanoplates and the mica substrate (Figure S12). Indexing the Laue pattern also permits deviatoric strain calculation of individual nanoplates of different thicknesses through comparison with the bulk, unstrained values (a = 8.856 Å, b = 8.577 Å, c = 12.472 Å, $\alpha = \beta = \gamma = 90^{o}$) (Figure S13). Laue patterns for a single $CsPbI_3$ nanoplate on Si/SiO_2 substrate match with bulk lattice parameters (Figure S14). Meanwhile, as the thickness of the nanoplates on mica decreases, the out-of-plane compressive strain increases (Figure 2D). The out-of-plane strain can be up to -0.42% for the thinnest plate we have measured, and is negligible for nanoplates above approximately 400 nm. The average out-of-plane strain for plates below 400 nm is -0.24%, and it is -0.033% for plates above 400 nm. This implies that as thickness decreases, there is greater strain and lattice distortion in the $CsPbI_3$ single crystalline nanoplates on mica substrates. In general, strain can originate from a number of factors in perovskite. Here, we consider two important factors that introduce strain and thus lattice distortion in our perovskite nanoplates: lattice mismatch and thermal expansion coefficient mismatch between the substrate and the adlayer. From our X-ray pole figures, we calculated the lattice mismatch between the perovskite

layer and the mica substrate to be -2.89%. As mentioned, this mismatch can cause the lattice of $CsPbI_3$ to dilate along the in-plane direction in order to match with the mica lattice. Additionally, we also need to take into account strain formation during cooling due to the large thermal expansion coefficient mismatch between the perovskites and the substrate.[19,36] Perovskite has a thermal expansion coefficient (α = 1.2 x 10^{-4} K^{-1})[37,38] that is orders of magnitude greater than that of the mica substrate (α = 8-12 x 10^{-6} K^{-1}).[39,40,41] At our synthesis temperature (360°C), both the perovskite and mica lattices are expanded and anchored to each other. When the growth is cooled to room temperature, the perovskite lattice tends to shrink to its lattice spacings at room temperature. However, the perovskite cannot contract efficiently due to the much smaller thermal expansion coefficient of mica, thus introducing tensile strain along the in-plane direction (Figure 2E). Owing to the positive Poisson's ratio in perovskites, the tensile in-plane strain can be compensated by out-of-plane lattice contraction,[20,21,36,42] which was observed in both our XRD and μXRD results. Similar strain formation behavior during cooling has been reported for $CsPbBr_3$ nanowires grown on sapphire substrates, where sapphires have a much smaller thermal expansion coefficient than that of perovskites.[36] In this reported work, the smaller thermal expansion coefficient of sapphire limits the contraction of perovskite lattice upon cooling, thereby causing the in-plane $CsPbBr_3$ lattice spacings to dilate at the sapphire interface. In this case, the in-plane strain can be accommodated by both out-of-plane lattice contraction and very large lattice rotations. In another work, the large thermal expansion coefficient mismatch between $MAPbI_3$ film and the ITO/glass substrate has also been reported to generate similar out-of-plane lattice shrinkage to compensate for tensile strain along the in-plane direction.[19]

Further evidence of strain was also confirmed with optical photoluminescence (PL) and Raman measurements. The PL emission for a region of high-T nanoplates grown on Si/SiO_2 is centered at 718 nm (1.73 eV), but this emission blueshifts to 712 nm (1.74 eV) for a region of high-T nanoplates with thickness heterogeneity on mica (Figure S15). We further measured PL spectra of individual nanoplates grown on mica and Si/SiO_2 using a confocal microscope with a 473 nm laser. Even though the dimensions of the nanoplates well exceed their quantum confinement regime, we observed a blueshift of PL peaks from 1.73 eV for a strain-free nanoplate on Si/SiO_2 (Figure S16) to 1.78 eV for the thinnest nanoplate on mica we can measure (Figure 3A). The PL peaks for individual nanoplates grown on mica gradually blueshift from 1.74 eV to 1.78 eV as the thickness decreases from 450 nm to 50 nm (Figure 3B). Although we were not able to grow nanoplates thinner than 50 nm on mica and characterize their PL peaks, we hypothesize that the bandgap will continue to increase as thickness decreases. Our results are consistent with the size-dependent bandgap modulation phenomenon attributed to strain.[32,36,43,44] Strain induces changes in the Pb—X—Pb bond lengths and bond angles, which would change the orbital overlaps and therefore band dispersion and bandgap. A similar thickness-dependent blueshift has been observed in $CsPbBr_3$ nanoplates grown on mica, and has been proposed to originate from the accumulated strain arising from a nontrivial strength of van der Waals epitaxial interaction between the soft perovskites and the mica substrate.[32] This blueshift behavior has also been studied in $CsPbBr_3$ nanowires grown on a sapphire substrate under similar epitaxial growth mechanism, where thinner nanowires were observed to have higher bandgap energies than thicker nanowires.[36] In the latter work, the authors confirmed this height-dependent bandgap modulation with TEM visualization of the lattice changes and attributed this behavior to large

lattice distortions from the changes in Pb—Br—Pb bond angle caused by heteroepitaxial strain in thinner nanowires. Additionally, we acquired low-frequency Raman spectra of individual nanoplates of different thicknesses on mica to observe the vibrational modes of the $[PbI_6]^{4-}$ octahedra. Low-frequency Raman spectra for the $CsPbI_3$ nanoplates showed distinct peaks that correspond to the vibrational modes of γ-$CsPbI_3$ reported in previous studies (Figure 3C, Figure S17).[45,46] For quantitative analysis, we performed least-square fitting of our Raman spectra with Lorentzian line shape functions to accurately determine the peak positions for different vibrational modes. Vibrational frequency is inversely correlated with bond length and can be used as a signature to probe strain. The low frequency modes between 20 cm^{-1} and 70 cm^{-1} can be attributed to the $[PbI_6]^{4-}$ octahedral bending motion.[45,47] Notably, the Raman peak centered at ~61 cm^{-1}, attributed to the equatorial bending of the I—Pb—I bonds, showed a redshift with decreasing nanoplate thickness (Figure 3D). This indicates a softening of the equatorial I—Pb—I bending mode, which can be a result of the increasing in-plane tensile strain for thinner nanoplates. On the other hand, a slight blueshift with decreasing nanoplate thickness was observed for the Raman peak at ~38 cm^{-1}, which is assigned to the axial bending of the I—Pb—I bonds (Figure 3E). This blueshift suggests a bond strengthening that restricts bending motion in this direction and can be explained by increasing out-of-plane compressive strain. Overall, the observed wavenumber shifts suggest that the Pb—I bonds fundamentally change as the nanoplate thickness decreases, an evidence of increasing strain for the thinner nanoplates.

Strain modulation can play a key role in enhancing the phase stability in perovskites, because strain can inherently alter the energetics of the competing phases. In $CsPbI_3$ polycrystalline thin

films, under unstrained conditions, the low-T phase is strongly energetically favored over the high-T phase, thereby creating a driving force for the high-T to low-T phase transition.[26] However, the introduction of strain shifts the relative energies for the two phases, resulting in a stabilization of the strained high-T phase. In this work, we sought to confirm whether the high-T phase stability enhancement previously observed in solution-processed $CsPbI_3$ polycrystalline thin films would still be upheld for our single-crystalline $CsPbI_3$ nanoplate model system. Differences in levels of grain boundaries, defect densities, size and epitaxial interaction with the substrate are all relevant factors that can modify the strain distribution between the two cases and may lead to different phase stability behaviors. Additionally, kinetically trapping the polycrystalline thin film after the synthesis is necessary to recover the strained high-T phase to study this strain-dependent phase transition, whereas the as-grown single-crystalline high-T $CsPbI_3$ nanoplate platform enables the intrinsic residual strain to be probed directly without any post-synthetic modifications. To investigate the effect of strain on the phase stability of single-crystalline high-T $CsPbI_3$ perovskite nanoplates, we studied the high-T to low-T phase transition at ambient conditions for nanoplates at different strain levels. The high-T perovskite phase is known to undergo phase transition to a low-T non-perovskite phase upon exposure to moisture (Figure 4A). As suggested by molecular dynamics (MD) simulations, the mechanism of the moisture-induced phase transition (MIPT) is due to moisture-induced halide vacancy creation at the perovskite surface.[16] A water layer adsorbed onto the perovskite surface can facilitate the high-T to low-T phase transition at room temperature by enhancing vacancy formation in the crystal lattice, thus lowering the high-T to low-T nucleation barrier and increasing the nucleation rate.[14,16] Using *in situ* PL optical microscopy, we can readily monitor this phase transformation

and determine the effect of strain on the phase stability of high-T $CsPbI_3$. The PL emission for an ensemble of high-T phase nanoplates grown on mica is centered at 712 nm (1.74 eV), while that of the low-T phase is at 467 nm (2.65 eV) (Figure 4B). The high-T to low-T phase transition kinetics at ambient conditions (21 ± 1°C, 50% ± 2% RH) can be quantified using *in situ* PL optical microscopy. A 620-nm light emitting diode (LED) was used to excite the crystal, while the emissions were collected with an optical microscope and an emission channel within 663 - 738 nm. Thus, the PL emission of high-T plates (bright) can be easily distinguished from that of low-T plates (dark), and a high-T to low-T phase transformation event is indicated by a complete disappearance of the bright emission. Representative PL images showing the time evolution of the high-T to low-T phase transition of a region of nanoplates grown on amorphous Si/SiO_2 and on mica exposed to ambient conditions over the course of one month are shown in Figure S18 and S19. About 48% of the plates epitaxially grown on mica still remained high-T phase after this time period, in contrast to the nanoplates grown on amorphous Si/SiO_2, where >90% of them transformed to low-T phase by the end of one month (Figure 4C, Figure S18-S19). This result demonstrates that the strained epitaxy at the perovskite-mica interface enhances the phase stability of single-crystalline $CsPbI_3$ nanoplates. Here, strain stems from a number of factors and shows a synergistic effect to phase transition. In addition to the lattice strain arising from the lattice mismatch and thermal expansion coefficient mismatch between perovskite and mica, strain also stems from the van der Waals epitaxy, which is significant enough to create a strong epilayer-substrate interaction to minimize the overall energy and enable lattice stabilization. The van der Waals forces can take up almost 27% of the surface interaction energy (approximately 20 meV/Å^2) in this system,[32] which is a considerable fraction of the chemical bond. The epitaxial

growth can provide a stabilization effect, since lattice constraints at the epitaxial interface would restrict atomic rearrangements during structural phase transition.[18] This result, combined with the enhanced phase stability also observed for $CsPbI_3$ polycrystalline thin film,[26] provides a generalization for the phase stability enhancement behavior under strain for $CsPbI_3$ materials. Applying strain to the $CsPbI_3$ crystal lattice would result in a strong energy destabilization of the low-T phase relative to the high-T phase, thereby inhibiting the high-T-to-low-T phase transition and enhancing the stability of the high-T phase. Controlling the thickness of the nanoplates also provides a direct approach to tune the accumulating strain at the interface and to measure phase stability under different levels of strain. We computed the fraction of nanoplates remaining in their high-T phase over the course of one month at ambient conditions for thick plates (>400 nm) and thin plates (<400 nm) grown on muscovite mica (Figure 4D). Representative PL images of a region of nanoplates on mica exposed to ambient conditions at 0 hours and the same nanoplates at 672 hours with their respective thickness distributions are shown in Figures 4E. Notably, while only ~31% of our thick plates remain high-T under ambient conditions at the end of one month after exposure, 56% of our thin nanoplate population maintain their high-T phase after this time period (Figure 4D). This difference in the thickness-dependent phase stability seems to be the greatest during the initial 15 hours, where a larger number of nanoplates above 400 nm transforms to low-T phase while the majority of nanoplates below 400 nm still remain high-T (Figure S20). This indicates that overall the thin nanoplates, which are more strained, have greater phase stability in ambient conditions compared to their thick counterparts. As the nanoplate thickness decreases, the relative crystal volume subjected to strain accumulated at the perovskite-substrate interface increases (Figure S21). Thus, thinner nanoplates undergo greater

relative lattice distortion and surface clamping with respect to their volume as compared to their thick counterpart, thus restricting structural rearrangements during phase transition and stabilizing the high-T phase. We note that even though 400 nm was used here as a cutoff for the thick and thin nanoplate populations based on the negligible strain observed for plates above 400 nm in our μXRD measurements, this is rather not the critical thickness of these nanoplates. The critical thickness is the thickness below which elastic strain can be accommodated without dislocation formation.[48] Beyond the critical thickness, dislocations start to form to partially relax strain. We expect the critical thickness for our $CsPbI_3$ nanoplates to be smaller than any thicknesses used in this study. Here, misfit dislocations were observed for nanoplates down to 150 nm (Figure S22), indicating that our nanoplates have surpassed the critical thickness limit and been partially relaxed during the epitaxial growth. Yet, the effect of the residual strain is still significant to enhance high-T phase stability. The residual strain continues to decrease as thickness increases until the nanoplates are fully relaxed, where they would have lower high-T phase stability.

Conclusions

In summary, we reported the presence of strain in our highly oriented growth of $CsPbI_3$ nanoplates on single crystal muscovite mica substrate. This strain varies with nanoplate thickness, and the strained epitaxy is found to enhance the high-T γ-phase stability of the nanoplates, most likely owing to the strain-induced energy destabilization for the low-T phase relative to the high-T phase. Here, the synergistic effect of strain to phase transition originates from a number of factors, including lattice mismatch, thermal expansion coefficient mismatch,

and ionic and van der Waals contributions to the strong substrate-lattice interaction. As lattice strain increases with decreasing nanoplate thickness, the nucleation rate from high-T to low-T phase reduces. This study provides a fundamental understanding of the intrinsic effect of lattice strain on phase transition and phase stabilization in a perovskite model system, which is necessary to drive further optimization and enhancement of perovskite-based optoelectronic device performance.

Experimental Procedures

Resource Availability

Lead Contact

Further information and requests for resources and reagents should be directed to and will be fulfilled by the lead contact, Peidong Yang (p_yang@berkeley.edu).

Materials Availability

This study did not generate new unique materials.

Data and Code Availability

All experimental data and code are available upon reasonable request to the lead contact.

Growth of $CsPbI_3$ nanoplates

$CsPbI_3$ nanoplates were grown via a one-step chemical vapor transport (CVT) process in a tube furnace (Lindberg/Blue M, Thermo Scientific). The precursors, cesium iodide (99.999% trace

metals basis, Aldrich) and lead(II) iodide (99%, Aldrich), were mixed in an alumina boat in a 1:1 molar ratio and placed at the center of the furnace in a 1-inch quartz tube. A freshly cleaved muscovite mica substrate (Grade V1, Electron Microscopy Sciences) was placed downstream at 8-12 cm away from the center. The precursors were then heated up from room temperature to 475°C for 10 minutes, and then kept at 475°C for 30 minutes. The furnace was then shut down and the growth was naturally cooled to room temperature. Ultra-high purity Ar gas (99.999%) was used as the carrier gas throughout the reaction with a flow rate of 100 sccm. The synthesis of $CsPbI_3$ nanoplates on Si/300nm SiO_2 also follows a similar procedure with slight modifications.[14,46] After the growth, samples were stored in an Ar-filled glovebox for further measurements.

Atomic Force Microscopy (AFM)

Nanoplate thicknesses were measured with an AFM (MFP-3D Asylum Research, Oxford Instruments) equipped with an acoustic isolation chamber (AEK 2002) and a non-conductive silicon probe (AC240TS-R3, Asylum Research, Oxford Instruments). Measurements were conducted in AC mode at a scan rate of 0.4 Hz with a resolution of 128x128 pixels.

Low-frequency (LF) Raman spectroscopy and microscopic photoluminescence (PL) measurement

Raman spectra of individual nanoplates were acquired using a Horiba LabRAM HR Evolution confocal microscope at the Stanford Nano Shared Facilities (SNSF) with a 100x, NA 0.9 microscope objective. A continuous wave 785 nm laser at a constant power density was focused onto each $CsPbI_3$ nanoplate, and the Raman scattered photons were collected with a diffraction

grating of 600 gr/mm and a spectrometer. The measured spectra were fitted with Lorentzian oscillators via the Multipeak Fitting 2 procedure in the IGOR Pro software.

PL spectra of individual nanoplates were acquired using a HORIBA LabRAMHR Evolution confocal microscope with a 473 nm laser under normal incidence and a 40x objective.

X-ray microdiffraction (μXRD), X-ray pole figure and powder X-ray diffraction (PXRD)

Synchrotron X-ray micro-fluorescence mapping (μXFM) and X-ray microdiffraction (μXRD) were performed at beamline 12.3.2 of the Advanced Light Source, Lawrence Berkeley National Laboratory (LBNL).[49] The nanoplate samples on their muscovite mica substrates were attached to the sample XYZ stage with double-sided tape. XFM and Laue patterns were obtained using polychromatic (pink) radiation with an energy range of 5-22 keV. The x-ray beam was focused to a size of 1x1 μm^2 via Kirkpatrick-Baez optics. XFM was obtained using a Vortex Si-drift detector. Laue patterns were collected using a DECTRIS Pilatus 1 M hybrid pixel detector placed at an angle of 60^o and a distance of 175 mm from the sample. The angle of incidence of the focused beam onto the sample was 25^o. Geometry of the experiment was calibrated using a Laue pattern obtained from a YAG crystal. The exposure time for each measurement was 1 second. The acquired Laue reflections were processed and indexed using the X-ray microdiffraction analysis software (XMAS)[50] to obtain the relative changes in lattice parameters, full deviatoric strain tensors and crystal orientations.

X-ray pole figures were obtained with a PANalytical Empyrean diffractometer at the Stanford Nano Shared Facilities (SNSF). The diffractometer was set up in a parallel beam geometry with a

Cu-source (λ_{ave} = 1.5419 Å). Parabolic mirror and parallel plate collimator were used as incident beam and diffracted beam optics, respectively. An X-ray pole figure contains information about the spatial distribution of plane normals for a specific set of equivalent planes {hkl} from all crystals irradiated in the sample. During the measurement, the sample is continuously rotated around its surface normal (azimuthal angle φ), and tilted with respect to the incoming beam (inclination angle ψ of the surface normal) while keeping 2θ constant. A polar contour map of the diffraction intensity is then plotted as a function of each tuple (φ, ψ), with ψ being the polar radius and φ the polar angle. Spots of enhanced intensities (poles) correspond to plane normals in the crystals to the pole direction defined by φ and ψ.

Powder X-ray diffraction (PXRD) patterns for a region of nanoplates grown on mica or Si/SiO_2 were measured with a Bruker AXS D8 Advance diffractometer with a Cu Kα ($\lambda_{K\alpha1}$ = 1.5406 Å, $\lambda_{K\alpha2}$ = 1.54439 Å) radiation source.

Moisture-dependent nucleation rate measurement

Time evolutions of moisture-induced phase transition of the nanoplates from the high-T phase to the low-T phase were captured over the course of one month in ambient conditions (21°C ± 1°C, 50% RH ± 2% RH). The temperature and RH level were monitored using a hygrometer (Honeywell) throughout the course of the experiment. The nanoplates were excited using a 620 nm wide-field light emitting diode (LED), and the emissions were collected with an optical microscope and a charge coupled device (CCD) camera and an emission channel within 663 nm-738 nm.

Acknowledgments

We are grateful for those who helped with this work: Dr. Denise Schichnes and Dr. Steven Ruzin for their microscopy support; John Grimsich for advice on XRD characterization and sample calibration.

This work was primarily supported by the U.S. Department of Energy, Office of Science, Office of Basic Energy Sciences, Materials Sciences and Engineering Division, under contract DE-AC02-05CH11231 within the Physical Chemistry of Inorganic Nanostructures Program (KC3103). H.K.D.L gratefully acknowledges support from the National Science Foundation's Graduate Research Fellowship Program (NSF GRFP) under grant DGE 1752814. J.J. and Y.Z. acknowledge the fellowship support from Suzhou Industrial Park. Part of this work used resources of the Advanced Light Source, which is a U.S. DOE Office of Science User Facility under contract DE-AC02-05CH1123. Phase transition kinetics measurements were performed at the U.C. Berkeley Biological Imaging Facility, supported in part by the National Institutes of Health S10 program under award 1S10RR026866-01. Low-frequency Raman spectroscopy and X-ray pole figure were both performed at the Stanford Nano Shared Facilities (SNSF), supported by the National Science Foundation under award ECCS-2026822.

Author Contributions

H.K.D.L. and P.Y. conceived the idea and designed the experiments. H.K.D.L. led the project involving materials synthesis, main characterizations (PXRD, AFM), optical measurements (Raman, PL), phase transition kinetics studies and data analysis. C.K.L helped with PL

measurements and provided insightful discussions for the project. N.T, H.K.D.L., Y.Z. conducted X-ray microdiffraction measurements and XMAS data analysis. A.V. conducted X-ray pole figures. J.J helped with EDX measurements. Z.L provided insightful discussions for synthesis and phase transition kinetics studies. H.K.D.L. and P.Y. wrote the manuscript. All authors contributed to writing or commented on the manuscript.

Declaration of Interests

The authors declare no competing interests.

References

(1) Kojima, A.; Teshima, K.; Shirai, Y.; Miyasaka, T. Organometal Halide Perovskites as Visible-Light Sensitizers for Photovoltaic Cells. *J. Am. Chem. Soc.* **2009**, *131* (17), 6050–6051. https://doi.org/10.1021/ja809598r.

(2) National Renewable Energy Laboratory. Best Research-Cell Efficiencies. **2019**.

(3) Green, M. A.; Ho-Baillie, A.; Snaith, H. J. The Emergence of Perovskite Solar Cells. *Nat. Photonics* **2014**, *8* (7), 506–514. https://doi.org/10.1038/nphoton.2014.134.

(4) Correa-Baena, J. P.; Saliba, M.; Buonassisi, T.; Grätzel, M.; Abate, A.; Tress, W.; Hagfeldt, A. Promises and Challenges of Perovskite Solar Cells. *Science (80-.).* **2017**, *358* (6364), 739–744. https://doi.org/10.1126/science.aam6323.

(5) Rong, Y.; Hu, Y.; Mei, A.; Tan, H.; Saidaminov, M. I.; Seok, S. Il; McGehee, M. D.; Sargent, E. H.; Han, H. Challenges for Commercializing Perovskite Solar Cells. *Science (80-.).* **2018**, *361* (6408). https://doi.org/10.1126/science.aat8235.

(6) Rühle, S. Tabulated Values of the Shockley-Queisser Limit for Single Junction Solar Cells. *Sol. Energy* **2016**, *130*, 139–147. https://doi.org/10.1016/j.solener.2016.02.015.

(7) Eperon, G. E.; Paternò, G. M.; Sutton, R. J.; Zampetti, A.; Haghighirad, A. A.; Cacialli, F.; Snaith, H. J. Inorganic Caesium Lead Iodide Perovskite Solar Cells. *J. Mater. Chem. A* **2015**, *3* (39), 19688–19695. https://doi.org/10.1039/c5ta06398a.

(8) Conings, B.; Drijkoningen, J.; Gauquelin, N.; Babayigit, A.; D'Haen, J.; D'Olieslaeger, L.; Ethirajan, A.; Verbeeck, J.; Manca, J.; Mosconi, E.; et al. Intrinsic Thermal Instability of Methylammonium Lead Trihalide Perovskite. *Adv. Energy Mater.* **2015**, *5* (15). https://doi.org/10.1002/aenm.201500477.

(9) Zhao, B.; Jin, S. F.; Huang, S.; Liu, N.; Ma, J. Y.; Xue, D. J.; Han, Q.; Ding, J.; Ge, Q. Q.; Feng, Y.; et al. Thermodynamically Stable Orthorhombic γ-CsPbI3 Thin Films for High-Performance Photovoltaics. *J. Am. Chem. Soc.* **2018**, *140* (37), 11716–11725. https://doi.org/10.1021/jacs.8b06050.

(10) Dastidar, S.; Hawley, C. J.; Dillon, A. D.; Gutierrez-Perez, A. D.; Spanier, J. E.; Fafarman, A. T. Quantitative Phase-Change Thermodynamics and Metastability of Perovskite-Phase Cesium Lead Iodide. *J. Phys. Chem. Lett.* **2017**, *8* (6), 1278–1282. https://doi.org/10.1021/acs.jpclett.7b00134.

(11) Sun, J. K.; Huang, S.; Liu, X. Z.; Xu, Q.; Zhang, Q. H.; Jiang, W. J.; Xue, D. J.; Xu, J. C.; Ma, J. Y.; Ding, J.; et al. Polar Solvent Induced Lattice Distortion of Cubic CsPbI3 Nanocubes and Hierarchical Self-Assembly into Orthorhombic Single-Crystalline Nanowires. *J. Am. Chem. Soc.* **2018**, *140* (37), 11705–11715. https://doi.org/10.1021/jacs.8b05949.

(12) Qiu, F.; Li, M.; Qi, J.; Jiang, Y.; Hu, J. Engineering Inorganic Lead Halide Perovskite Deposition toward Solar Cells with Efficiency Approaching 20%. *Aggregate* **2021**, *2* (1), 66–83. https://doi.org/10.1002/agt2.19.

(13) Steele, J. A.; Lai, M.; Zhang, Y.; Lin, Z.; Hofkens, J.; Roeffaers, M. B. J.; Yang, P. Phase Transitions and Anion Exchange in All-Inorganic Halide Perovskites. *Accounts of Materials Research*. 2020, pp 3–15. https://doi.org/10.1021/accountsmr.0c00009.

(14) Lin, Z.; Zhang, Y.; Gao, M.; Steele, J. A.; Louisia, S.; Yu, S.; Quan, L. N.; Lin, C. K.; Limmer, D. T.; Yang, P. Kinetics of Moisture-Induced Phase Transformation in Inorganic Halide Perovskite. *Matter* **2021**, *4* (7), 2392–2402. https://doi.org/10.1016/j.matt.2021.04.023.

(15) Lin, C. K.; Zhang, Y.; Gao, M.; Lin, J. A.; Le, H. K. D.; Lin, Z.; Yang, P. Controlling the Phase Transition in CsPbI3Nanowires. *Nano Lett.* **2022**, *22* (6), 2437–2443. https://doi.org/10.1021/acs.nanolett.2c00170.

(16) Lin, J.; Lai, M.; Dou, L.; Kley, C. S.; Chen, H.; Peng, F.; Sun, J.; Lu, D.; Hawks, S. A.; Xie, C.; et al. Thermochromic Halide Perovskite Solar Cells. *Nat. Mater.* **2018**, *17* (3), 261–267. https://doi.org/10.1038/s41563-017-0006-0.

(17) Gao, M.; Zhang, Y.; Lin, Z.; Jin, J.; Folgueras, M. C.; Yang, P. The Making of a Reconfigurable Semiconductor with a Soft Ionic Lattice. *Matter* **2021**, *4* (12), 3874–3896. https://doi.org/10.1016/j.matt.2021.09.023.

(18) Chen, Y.; Lei, Y.; Li, Y.; Yu, Y.; Cai, J.; Chiu, M. H.; Rao, R.; Gu, Y.; Wang, C.; Choi, W.; et al. Strain Engineering and Epitaxial Stabilization of Halide Perovskites. *Nature* **2020**, *577* (7789), 209–215. https://doi.org/10.1038/s41586-019-1868-x.

(19) Zhao, J.; Deng, Y.; Wei, H.; Zheng, X.; Yu, Z.; Shao, Y.; Shield, J. E.; Huang, J. Strained Hybrid Perovskite Thin Films and Their Impact on the Intrinsic Stability of Perovskite Solar Cells. *Sci. Adv.* **2017**, *3* (11). https://doi.org/10.1126/sciadv.aao5616.

(20) Kim, H. S.; Park, N. G. Importance of Tailoring Lattice Strain in Halide Perovskite Crystals. *NPG Asia Mater.* **2020**, *12* (1). https://doi.org/10.1038/s41427-020-00265-w.

(21) Liu, D.; Luo, D.; Iqbal, A. N.; Orr, K. W. P.; Doherty, T. A. S.; Lu, Z. H.; Stranks, S. D.; Zhang, W. Strain Analysis and Engineering in Halide Perovskite Photovoltaics. *Nat. Mater.* **2021**, *20* (10), 1337–1346. https://doi.org/10.1038/s41563-021-01097-x.

(22) Wang, L.; King, I.; Chen, P.; Bates, M.; Lunt, R. R. Epitaxial and Quasiepitaxial Growth of Halide Perovskites: New Routes to High End Optoelectronics. *APL Mater.* **2020**, *8* (10). https://doi.org/10.1063/5.0017172.

(23) Yu, H.; Sun, Q.; Zhang, T.; Zhang, X.; Shen, Y.; Wang, M. Is the Strain Responsible to Instability of Inorganic Perovskites and Their Photovoltaic Devices? *Mater. Today Energy* **2021**, *19*, 1–12. https://doi.org/10.1016/j.mtener.2020.100601.

(24) Moloney, E. G.; Yeddu, V.; Saidaminov, M. I. Strain Engineering in Halide Perovskites. *ACS Mater. Lett.* **2020**, *2* (11), 1495–1508. https://doi.org/10.1021/acsmaterialslett.0c00308.

(25) Saidaminov, M. I.; Kim, J.; Jain, A.; Quintero-Bermudez, R.; Tan, H.; Long, G.; Tan, F.; Johnston, A.; Zhao, Y.; Voznyy, O.; et al. Suppression of Atomic Vacancies via Incorporation of Isovalent Small Ions to Increase the Stability of Halide Perovskite Solar Cells in Ambient Air. *Nat. Energy* **2018**, *3* (8), 648–654. https://doi.org/10.1038/s41560-018-0192-2.

(26) Steele, J. A.; Jin, H.; Dovgaliuk, I.; Berger, R. F.; Braeckevelt, T.; Yuan, H.; Martin, C.; Solano, E.; Lejaeghere, K.; Rogge, S. M. J.; et al. Thermal Unequilibrium of Strained Black CsPbI3 Thin Films. *Science (80-.).* **2019**, *365* (6454), 679–684. https://doi.org/10.1126/science.aax3878.

(27) Zhao, Y.; Miao, P.; Elia, J.; Hu, H.; Wang, X.; Heumueller, T.; Hou, Y.; Matt, G. J.; Osvet, A.; Chen, Y. T.; et al. Strain-Activated Light-Induced Halide Segregation in Mixed-Halide Perovskite Solids. *Nat. Commun.* **2020**, *11* (1), 1–9. https://doi.org/10.1038/s41467-020-20066-7.

(28) Kim, G.; Min, H.; Lee, K. S.; Lee, D. Y.; Yoon, S. M.; Seok, S. Il. Impact of Strain Relaxation on Performance of A-Formamidinium Lead Iodide Perovskite Solar Cells. *Science (80-.).* **2020**, *370* (6512), 108–112. https://doi.org/10.1126/science.abc4417.

(29) Zhu, C.; Niu, X.; Fu, Y.; Li, N.; Hu, C.; Chen, Y.; He, X.; Na, G.; Liu, P.; Zai, H.; et al. Strain Engineering in Perovskite Solar Cells and Its Impacts on Carrier Dynamics. *Nat. Commun.* **2019**, *10* (1). https://doi.org/10.1038/s41467-019-08507-4.

(30) Wang, Y.; Jia, C.; Fan, Z.; Lin, Z.; Lee, S. J.; Atallah, T. L.; Caram, J. R.; Huang, Y.; Duan, X. Large-Area Synthesis and Patterning of All-Inorganic Lead Halide Perovskite Thin Films and Heterostructures. *Nano Lett.* **2021**, *21* (3), 1454–1460. https://doi.org/10.1021/acs.nanolett.0c04594.

(31) Chen, J.; Fu, Y.; Samad, L.; Dang, L.; Zhao, Y.; Shen, S.; Guo, L.; Jin, S. Vapor-Phase Epitaxial Growth of Aligned Nanowire Networks of Cesium Lead Halide Perovskites (CsPbX3, X = Cl, Br, I). *Nano Lett.* **2020**, *17* (1), 460–466. https://doi.org/10.1021/acs.nanolett.6b04450.

(32) Wang, Y.; Gao, L.; Yang, Y.; Xiang, Y.; Chen, Z.; Dong, Y.; Zhou, H.; Cai, Z.; Wang, G. C.; Shi, J. Nontrivial Strength of van Der Waals Epitaxial Interaction in Soft Perovskites. *Phys. Rev. Mater.* **2018**, *2* (7). https://doi.org/10.1103/PhysRevMaterials.2.076002.

(33) Zhang, Q.; Su, R.; Liu, X.; Xing, J.; Sum, T. C.; Xiong, Q. High-Quality Whispering-Gallery-Mode Lasing from Cesium Lead Halide Perovskite Nanoplatelets. *Adv. Funct. Mater.* **2016**, *26* (34), 6238–6245. https://doi.org/10.1002/adfm.201601690.

(34) Sutton, R. J.; Filip, M. R.; Haghighirad, A. A.; Sakai, N.; Wenger, B.; Giustino, F.; Snaith, H. J. Cubic or Orthorhombic? Revealing the Crystal Structure of Metastable Black-Phase CsPbI3 by Theory and Experiment. *ACS Energy Lett.* **2018**, *3* (8), 1787–1794. https://doi.org/10.1021/acsenergylett.8b00672.

(35) Wu, J.; Liu, S. C.; Li, Z.; Wang, S.; Xue, D. J.; Lin, Y.; Hu, J. S. Strain in Perovskite Solar Cells: Origins, Impacts and Regulation. *National Science Review*. Oxford University Press August 1, 2021. https://doi.org/10.1093/nsr/nwab047.

(36) Oksenberg, E.; Merdasa, A.; Houben, L.; Kaplan-Ashiri, I.; Rothman, A.; Scheblykin, I. G.; Unger, E. L.; Joselevich, E. Large Lattice Distortions and Size-Dependent Bandgap Modulation in Epitaxial Halide Perovskite Nanowires. *Nat. Commun.* **2020**, *11* (1), 1–11. https://doi.org/10.1038/s41467-020-14365-2.

(37) Ke, F.; Wang, C.; Jia, C.; Wolf, N. R.; Yan, J.; Niu, S.; Devereaux, T. P.; Karunadasa, H. I.; Mao, W. L.; Lin, Y. Preserving a Robust CsPbI3 Perovskite Phase via Pressure-Directed Octahedral Tilt. *Nat. Commun.* **2021**, *12* (1), 1–8. https://doi.org/10.1038/s41467-020-20745-5.

(38) Trots, D. M.; Myagkota, S. V. High-Temperature Structural Evolution of Caesium and

Rubidium Triiodoplumbates. *J. Phys. Chem. Solids* **2008**, *69* (10), 2520–2526. https://doi.org/10.1016/j.jpcs.2008.05.007.

(39) Goldstein, L.; Post, B. Thermal Expansion Coefficients of Ruby Muscovite Mica. *J. Appl. Phys.* **1969**, *40* (7), 3056–3057. https://doi.org/10.1063/1.1658130.

(40) Zhao, F.; Wang, B.; Cui, X.; Pan, N.; Wang, H.; Hou, J. G. Buckle Delamination of Textured TiO2 Thin Films on Mica. *Thin Solid Films* **2005**, *489* (1–2), 221–228. https://doi.org/10.1016/j.tsf.2005.04.075.

(41) McNeil, L. E.; Grimsditch, M. Elastic Moduli of Muscovite Mica. *J. Phys. Condens. Matter* **1993**, *5* (11), 1681–1690. https://doi.org/10.1088/0953-8984/5/11/008.

(42) Wu, J.; Liu, S. C.; Li, Z.; Wang, S.; Xue, D. J.; Lin, Y.; Hu, J. S. Strain in Perovskite Solar Cells: Origins, Impacts and Regulation. *Natl. Sci. Rev.* **2021**, *8* (8). https://doi.org/10.1093/nsr/nwab047.

(43) Oksenberg, E.; Sanders, E.; Popovitz-Biro, R.; Houben, L.; Joselevich, E. Surface-Guided CsPbBr3 Perovskite Nanowires on Flat and Faceted Sapphire with Size-Dependent Photoluminescence and Fast Photoconductive Response. *Nano Lett.* **2018**, *18* (1), 424–433. https://doi.org/10.1021/acs.nanolett.7b04310.

(44) Li, D.; Wang, G.; Cheng, H.-C.; Chen, C.-Y.; Wu, H.; Liu, Y.; Huang, Y.; Duan, X. Size-Dependent Phase Transition in Methylammonium Lead Iodide Perovskite Microplate Crystals. *Nat. Commun.* **2016**, *7* (1), 11330. https://doi.org/10.1038/ncomms11330.

(45) Yang, Y.; Robbins, J. P.; Ezeonu, L.; Ma, Y.; Sparta, N.; Kong, X.; Strauf, S.; Podkolzin, S. G.; Lee, S. S. Probing Lattice Vibrations of Stabilized CsPbI3polymorphs: Via Low-Frequency Raman Spectroscopy. *J. Mater. Chem. C* **2020**, *8* (26), 8896–8903.

https://doi.org/10.1039/d0tc02123g.

(46) Lin, Z.; Folgueras, M. C.; Le, H. K. D.; Gao, M.; Yang, P. Laser-Accelerated Phase Transformation in Cesium Lead Iodide Perovskite. *Matter* **2022**, *5* (5), 1455–1465. https://doi.org/10.1016/j.matt.2022.04.002.

(47) Badrooj, M.; Jamali-Sheini, F.; Torabi, N. Optoelectronic Properties of Mixed Sn/Pb Perovskite Solar Cells: The Study of Compressive Strain by Raman Modes. *J. Phys. Chem. C* **2020**, *124* (49), 27136–27147. https://doi.org/10.1021/acs.jpcc.0c07999.

(48) Pohl, U. W. *Epitaxy of Semiconductors: Introduction to Physical Principles*; Springer Berlin, Heidelberg, 2013.

(49) Tamura, N.; Kunz, M.; Chen, K.; Celestre, R. S.; MacDowell, A. A.; Warwick, T. A Superbend X-Ray Microdiffraction Beamline at the Advanced Light Source. *Mater. Sci. Eng. A* **2009**, *524* (1–2), 28–32. https://doi.org/10.1016/j.msea.2009.03.062.

(50) Tamura, N. XMAS: A Versatile Tool for Analyzing Synchrotron X-Ray Microdiffraction Data. *Strain Dislocation Gradients from Diffr. Spat. Local Struct. Defects* **2014**, 125–155. https://doi.org/10.1142/9781908979636_0004.

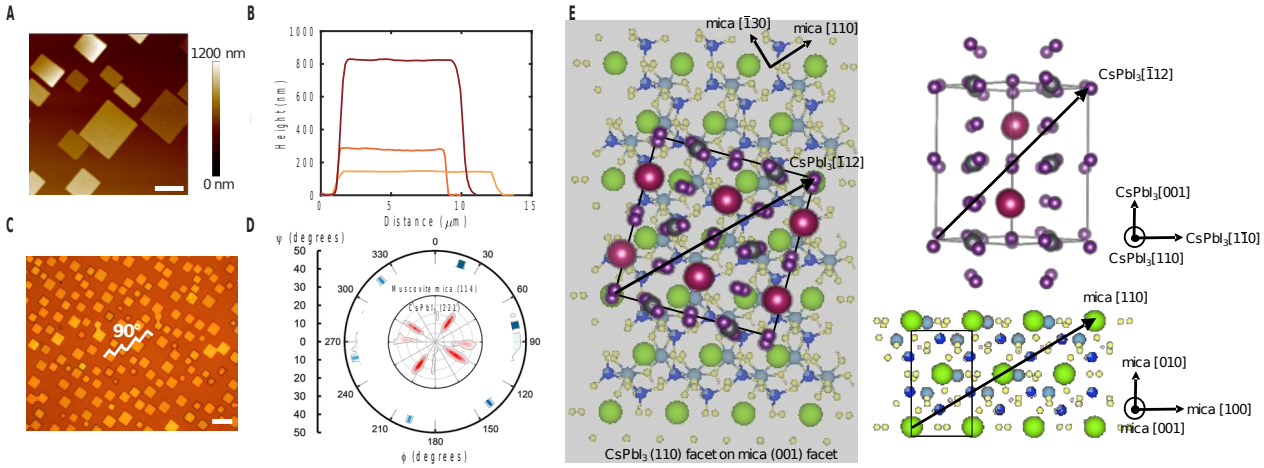

Figure 1. Characterization of $CsPbI_3$ nanoplates epitaxially grown on muscovite mica substrate. **(A)** AFM image of $CsPbI_3$ nanoplates grown on mica. Scale bar: 10 μm. **(B)** Representative AFM height profiles of individual $CsPbI_3$ nanoplates. **(C)** Optical microscopy image of $CsPbI_3$ nanoplates grown on mica. Scale bar: 20 μm. **(D)** X-ray pole figure of mica(114) (blue) overlaid with the pole figure of $CsPbI_3$ (221) (red). **(E)** (Right) Schematic illustration of the atomic arrangement of γ-$CsPbI_3$ (110) (dark grey: Pb, pink: Cs, purple: I) on the (001) plane of muscovite mica (green: K, dark blue: Si, light blue: Al, yellow: O, pink: H) and the proposed incommensurate epitaxial relationship. (Left) γ-$CsPbI_3$ (110) facet and muscovite mica (001) facet, with black outlines marking one unit cell of each crystal structure.

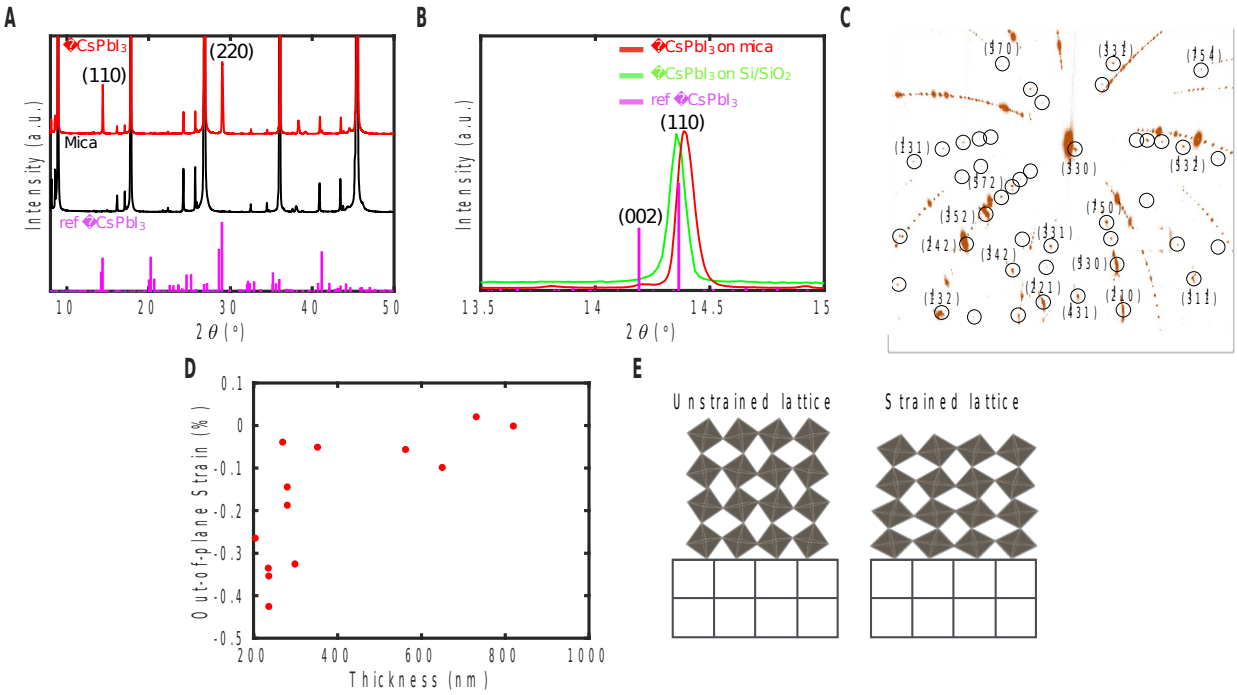

Figure 2. Structural characterizations of strain in $CsPbI_3$ nanoplates. **(A)** Powder X-ray diffraction (PXRD) patterns of a region of high-T $CsPbI_3$ nanoplates grown on muscovite mica (red, top), and muscovite mica (black, middle). Bottom purple bar graph represents the reference pattern for high-T γ-phase $CsPbI_3$ structure from Sutton *et al.*[34] **(B)** Magnified PXRD patterns in the 13.5°-15° 2θ range for $CsPbI_3$ nanoplates grown on muscovite mica (red) and on Si/SiO_2 substrate (green). Purple bars represent the reference pattern for high-T γ-phase $CsPbI_3$ from Sutton *et al*[34] in this 2θ range. **(C)** Representative Laue reflection pattern of an individual high-T γ-phase $CsPbI_3$ nanoplate grown on muscovite mica. **(D)** Thickness-dependent out-of-plane strains of individual high-T γ-phase $CsPbI_3$ nanoplates grown on muscovite mica. **(E)** Schematic illustration of the strained $CsPbI_3$ lattice on muscovite mica, showing out-of-plane compressive strain and in-plane tensile strain relative to the unstrained $CsPbI_3$ lattice.

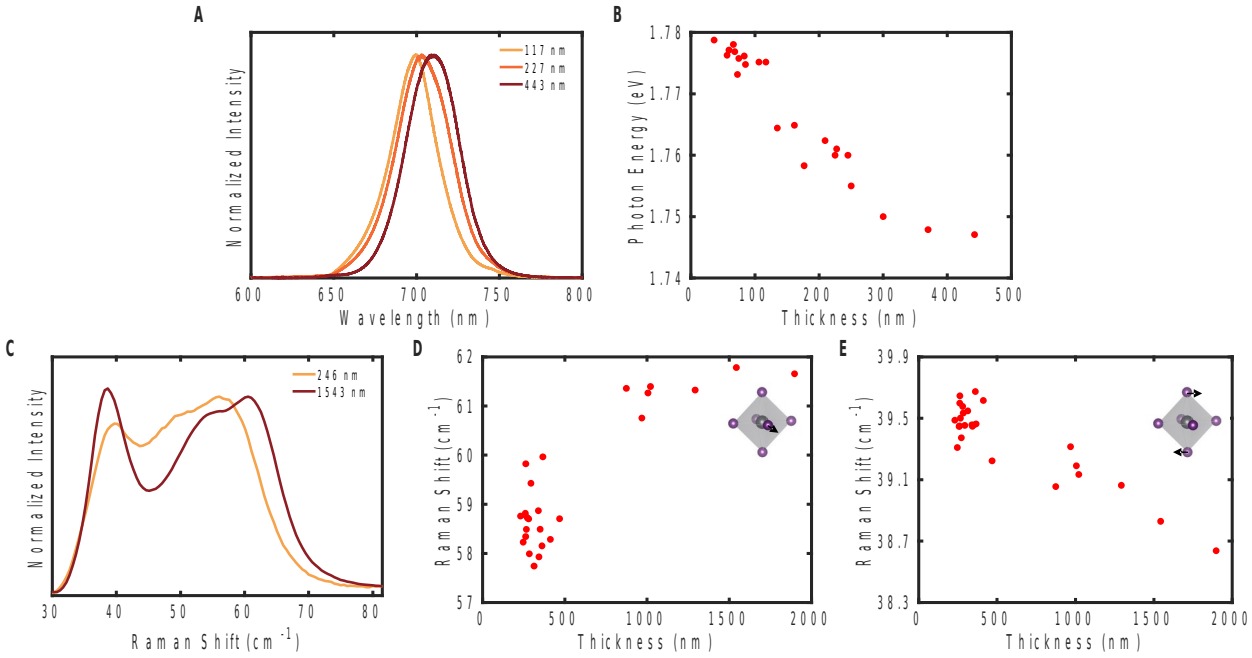

Figure 3. Optical characterizations of strain in individual $CsPbI_3$ nanoplates of different thicknesses. **(A)** Representative photoluminescence spectra of individual high-T γ-phase $CsPbI_3$ nanoplates of different thicknesses (117 nm, 227 nm, 443 nm) on muscovite mica. A blueshift of the photoluminescence peaks with decreasing nanoplate thickness is observed and attributed to increasing strain. **(B)** Thickness-dependent bandgap of high-T γ-phase $CsPbI_3$ nanoplates grown on muscovite mica. **(C)** Representative confocal Raman spectra (λ_{ex}= 785 nm) of individual high-T γ-phase $CsPbI_3$ nanoplates of different thicknesses (246 nm, 1543 nm) on muscovite mica. **(D)** Thickness-dependent Raman shift for the I—Pb—I equatorial bending mode of high-T γ-phase $CsPbI_3$ nanoplates grown on muscovite mica (inset: schematic illustration of the I—Pb—I equatorial bending mode). **(E)** Thickness-dependent Raman shift for the I—Pb—I axial bending mode of high-T γ-phase $CsPbI_3$ nanoplates grown on muscovite mica (inset: schematic illustration of the I—Pb—I axial bending mode).

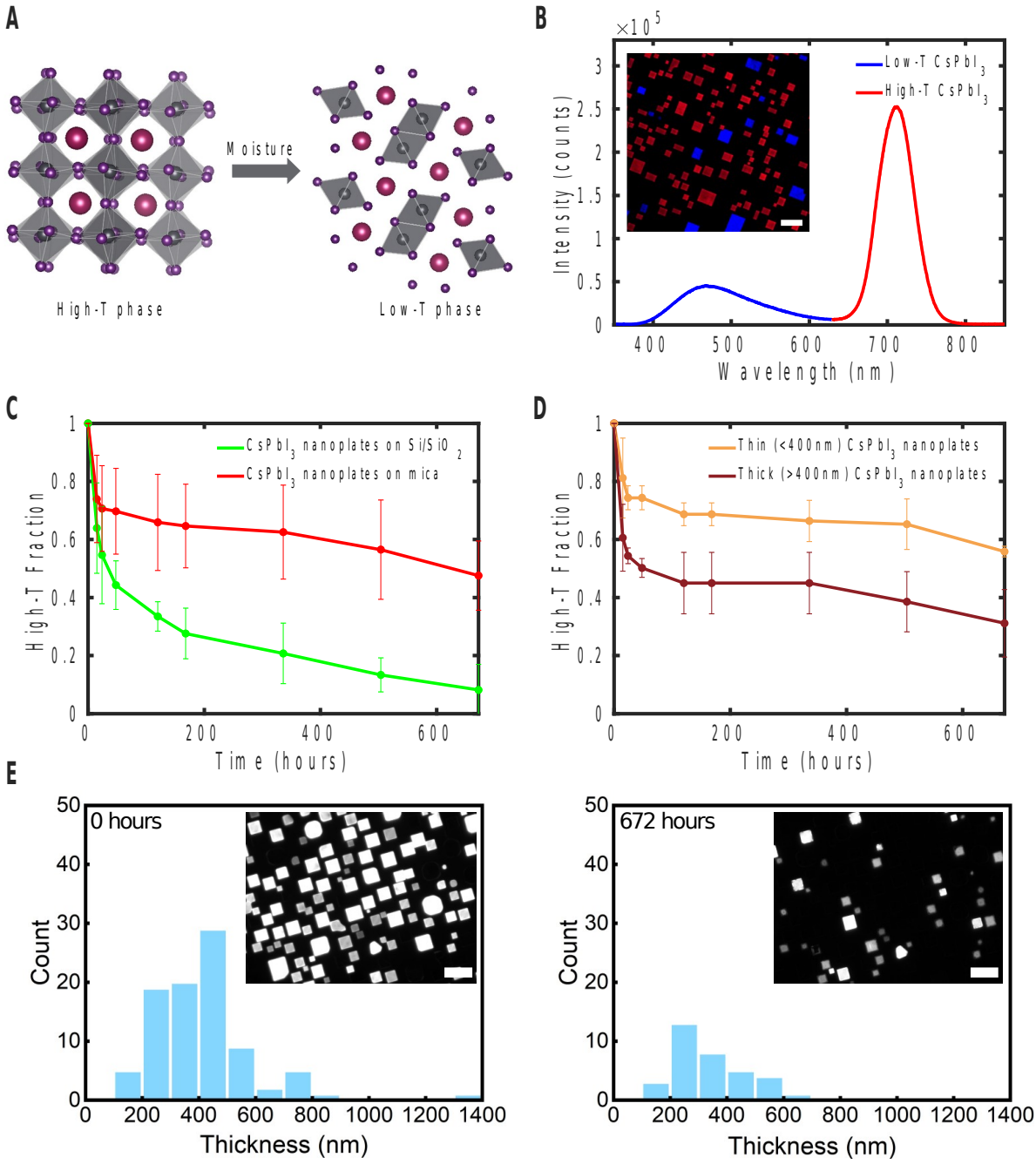

Figure 4. Strain stabilization of high-T γ-phase $CsPbI_3$ nanoplates grown on muscovite mica. (**A**) Schematic illustration of the phase transition of high-T γ-phase $CsPbI_3$ into low-T δ-phase $CsPbI_3$ upon exposure to moisture. (**B**) Photoluminescence spectra and image (inset) of high-T γ-phase $CsPbI_3$ nanoplates (red) and low-T δ-phase $CsPbI_3$ nanoplates (blue) grown on muscovite

mica. Scale bar: 15 μm. **(C)** Fractions of remaining high-T $CsPbI_3$ nanoplates on muscovite mica (red) and on Si/SiO_2 (green) over the course of 672 hours (one month) at ambient conditions (21 ± 1°C, 50% ± 2% RH). **(D)** Fractions of remaining thin (< 400 nm, dark red) and thick (> 400 nm, orange) high-T $CsPbI_3$ nanoplates on muscovite mica over the course of 672 hours (one month) at ambient conditions (21 ± 1°C, 50% ± 2% RH). The fraction of remaining high-T nanoplates at each timepoint is averaged over three samples, with error bars reflecting one standard deviation. **(E)** Representative photoluminescence images (λ_{ex}= 620 nm, emission channel: 663 nm - 738 nm) of $CsPbI_3$ nanoplates on muscovite mica at ambient conditions (21 ± 1°C, 50% ± 2% RH) at 0 hours and the same nanoplates at 672 hours (insets, scale bars: 20 μm), with respective thickness distributions of the remaining high-T nanoplates.